Fusion Behavior of Pure Magnesium During Selective Laser Melting

Snehashis Pal^{1,2} ⊠ – Matjaž Finšgar¹ – Jernej Vajda³ – Uroš Maver³ – Tomaž Brajlih² – Nenad Gubeljak² – Hanuma Reddy Tiyyagura⁴ – Igor Drstvenšek²

- 1 Faculty of Chemistry and Chemical Engineering, University of Maribor, Slovenia
- 2 Faculty of Mechanical Engineering, University of Maribor, Slovenia
- 3 Faculty of Medicine, University of Maribor, Slovenia
- 4 Institute of Optoelectronics, Military University of Technology, Poland
- snehashis.pal@um.si.

Abstract This study examined the melting behavior and flowability of pure magnesium during selective laser melting. The potential to increase product density was also investigated. Various combinations of manufacturing parameters were considered. The laser power was gradually increased in different machine runs, with different scanning speeds for each run to vary the energy density (ED). The laser power ranged from 10 W to 75 W, and the scanning speed ranged from 100 mm/s to 800 mm/s. Lower laser powers resulted in poor melting, while higher laser powers produced better melting, with significant differences even when the ED was the same. High EDs between 3.50 J/mm² and 4.30 J/mm² led to a lack of melting at low laser power and to an unstable melt pool with significant spattering at high laser power. In contrast, moderate EDs in the range of 1.40 J/mm² to 2.90 J/mm² resulted in better density at high laser power. Higher scanning speeds helped to avoid the formation of a dense smog cloud and provided sufficient energy in a short time with the aid of higher laser power. Therefore, increasing both laser power and scanning speed improved melting performance and increased product density. The relative product density ranged from 80 % to 96.5 %. Reducing the layer thickness from 50 µm to 25 µm at a laser power of 40 W resulted in the formation of a well-formed melt pool in some areas and significant melt spattering in others, which led to a deterioration in density.

Keywords magnesium, melt pool, laser power, scanning speed, layer thickness, support structure, laser powder bed fusion

Highlights

- The fusion and pore formation of Mg during the selective laser melting process were investigated.
- Higher energy density (ED) may cause a lack of melting than lower ED due to the high smog formation.
- Higher scanning speed with higher laser power can avoid the smog cloud and perform better fusion.
- Reducing the layer thickness from 50 μm to 25 μm led to improved melting or massive spattering.

1 INTRODUCTION

Lightweight materials are essential for a range of applications, particularly in the automotive, aerospace, and electronics industries [1,2]. Reducing component weight can significantly improve overall performance and fuel efficiency [3]. In medical implants, especially for orthopedic applications, lightweight and biodegradable materials are vital [4,5]. Their lightness aids patient mobility, while biodegradability eliminates the need for a second surgery by allowing the implant to dissolve naturally in the body over time [6.7]. Magnesium (Mg) and its alloys are increasingly favored due to their properties, which meet these stringent requirements [8,9]. Mg is not only very light but also offers promising biodegradability and high biocompatibility [10,11]. Mg and Mg-alloys allow regulation of mechanical and corrosive properties, making them suitable for biomedical applications [12]. Furthermore, the mechanical properties of magnesium alloys are similar to those of bone, which is advantageous for orthopedic implants [13].

Despite these benefits, Mg has certain drawbacks, such as a lower melting point and higher reactivity to oxygen and moisture compared to other metals [14,15]. In various applications, proper handling and alloying are required to address these challenges [16,17]. Traditional manufacturing processes have limitations in this regard [18]. However, additive manufacturing (AM) processes offer much greater flexibility than conventional methods [19,20]. AM

provides a protective environment for the manufacturing process and enables in-situ alloying, which is crucial when working with reactive materials like magnesium. It can transform complex computer-aided design (CAD) models into single or multiple products, supporting customization and intricate designs [21]. Selective laser melting (SLM), also known as laser powder bed fusion (LPBF), is one of the most popular metal AM technologies for manufacturing metal products [22]

SLM uses an inert gas to reduce the oxygen content in the process chamber, requiring a continuous flow of this gas to maintain the desired oxygen levels [23]. In this process, a laser melts the metal powder track by track and layer by layer [24,25]. The powder particles, typically with diameters of several dozen micrometers, build up the product layer by layer, with each layer usually being 20 to 100 micrometers thick [26,27]. Rapid heating, melting, mixing, and solidification occur during the fusion process in SLM [28,29]. Using Mg in SLM presents significant challenges due to its low melting and boiling points and high flammability [30]. Rapid heating can lead to vaporization and combustion of Mg [2]. The small temperature difference between the melting and boiling points causes the melt pool to become unstable [31]. Additionally, the lightweight nature of Mg poses a problem as it can be easily carried away by inert gas, leading to material loss and the formation of smog that obstructs the laser's operation [16]. These issues significantly affect the SLM

process, as material loss from the action zone and smog formation hinder the laser's ability to function effectively [32].

To address these challenges, this study investigated the interactions between the laser and Mg, as well as the thermophysical properties of the melt pools and solidification during the SLM manufacturing process. There are several results in the literature on the density of Mg-alloys fabricated by SLM, but only a few studies focus on improving the density of pure Mg products. To our knowledge, and according to the report by Zeng et al. [33], there is no literature in which a relative density of 98 % was achieved for Mg parts produced by the SLM process. Therefore, in this study, the laser powers and scanning speeds were initially selected based on previous studies by Hu et al. [34] and Yang et al. [5]. Hu et al. [34] obtained the best relative height density of 96.13 % at a high energy density (ED) with a laser power and scanning speed of 90 W and 100 mm/s, respectively. On the other hand, Yang et al. [5] obtained useful results at laser powers and scanning speeds between 20 W to 100 W and 100 mm/s to 900 mm/s. Therefore, this study started with a scanning speed of 100 mm/s and a laser power of 10 W to keep the ED within a suitable range. Observations and analyses from this initial phase served as a basis for selecting different combinations of laser power and scanning speed to further investigate these phenomena and achieve better metallurgical properties.

This comprehensive approach aimed to optimize the SLM process for Mg, focusing on understanding and mitigating issues related to rapid heating, material loss, and smog formation. By exploring the effects of different combinations of laser powers and scanning speeds, the study sought to enhance the metallurgical properties of the produced components, paving the way for more effective use of Mg in SLM processes.

2 METHODS AND MATERIALS

2.1 Material

The samples were produced using pure magnesium powder from Nanografi Nano Technology (Germany), and the manufacturing characteristics were analyzed. The spherical powder particles ranged in size from 35 μ m to 50 μ m, with 5 % of the particles outside this range. After production by centrifugal atomization, the powder was packaged in an inert gas environment. The powder was unsealed to fill the filling chamber after the oxygen concentration was reduced to less than 0.01 % using argon.

2.2 Machining Chamber

The manufacturing behavior was studied using the Arrow Metal Printing – LMP200 SLM machine supplied by Dentas, Slovenia. Argon was used to reduce the oxygen content in the chamber and to keep the O2 level below 10 ppm during sample production. An O2 sensor monitored and automatically adjusted the O2 level by adding argon to the machining chamber when it exceeded 10 ppm. As magnesium is very light, the processing environment contained Mg powder and its fumes. To remove these, the chamber gases were circulated and passed through a filter at a flow rate of 280 L/min. Before production runs began, the laser system was calibrated and a sensor monitored the current laser power. To maintain heat conduction and the material bond between the build plate and the support, the build plate was made of magnesium.

2.2 Support Structure

Several cubic test specimens measuring $6 \text{ mm} \times 6 \text{ mm} \times 6 \text{ mm}$ were produced for each test condition. As magnesium has good thermal

conductivity and a very high coefficient of thermal expansion (CTE of $26 \times 10^{-6}~\rm K^{-1}$), large thermal stresses and volume changes occur during the SLM process, causing the part to shrink, bend, and eventually self-destruct. Therefore, three types of support structures were used to hold the samples firmly. As shown in Fig. 1, fabrication of the specimens began with 2 mm high supports. In this study, a support structure typically used for the fabrication of stronger materials such as Ti-6Al-4V and AlSi10Mg was employed (see Fig. 1a). This support beam has a smaller diameter neck that facilitates separation of the fabricated part from the support beams. Twenty-five (5 × 5) support beams were placed under the 6 mm × 6 mm base of the cubes.

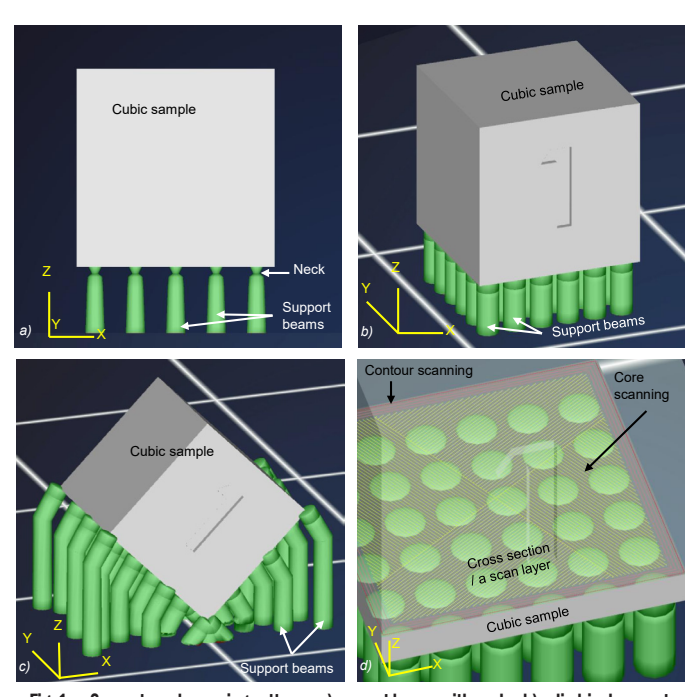


Fig. 1. Supports and scanning patterns; a) support beams with necks, b) cylindrical support beams, c) samples with different orientations, and d) scanning pattern

In this study, the effects of laser parameters at different layer thicknesses and their melting properties with existing supports were investigated. The manufacturing process is costly due to the use of argon and the risk that the failure of a single sample can cause the failure of several samples in the same build. If one sample fails, it can hinder the movement of the recoater, requiring the entire process to be stopped and restarted from the beginning. This research aimed to find a solution to the manufacturing problem when supports are present, as supports are often necessary for the actual production of the part. It is easier to remove samples from the build plate and prepare a smooth build plate again than to produce samples without support. Therefore, in addition to analyzing melting properties, the effect of support, including different support designs, is also examined and reported in this article.

Since the support beam with a neck was not able to prevent the piece from bending, cylindrical beams were used, as shown in Fig. 1b. The beams had diameters of 0.4 mm, with a 6×6 array of beams under the 6 mm \times 6 mm base of the cubes. Although this support structure was sufficient to prevent most specimens from bending, some specimens still bent or detached from the supports after a few layers were fabricated.

As some specimens bent and moved away from the cylindrical support beams, the orientation of the specimens was changed, as shown in Fig. 1c. However, this orientation increased the bottom surface area, leading to a more uneven surface at the start of

fabrication. Although this support structure held the part firmly in place, the uneven shape and surface formation of the specimens led to the decision in this study to align the cubic specimens so that their base surface remained horizontal. Ultimately, cylindrical support beams are best suited to hold the part when the base of a cubic sample is horizontal.

2.3 Scanning Patterns

The scanning pattern consisted of four successive contours and a checkerboard core scanning pattern, as shown in Fig. 1d. As the area to be scanned for each layer was approximately 6 mm × 6 mm, four sub-squares were scanned in a checkerboard arrangement. Each square was scanned with multiple laser scan tracks, with a 50 % overlap between tracks. The diameter of the laser spot was 70 μm; therefore, the hatch spacing was 35 μm. A larger hatch spacing resulted in a lower product density. Two consecutive scanning tracks were scanned in opposite directions. The scanning tracks were rotated by 60° for successive layers during manufacture. The Yb:glass fiber laser was always focused perpendicular to the powder bed using a telecentric F-theta lens. The telecentric F-theta lens combines the flat-field focusing of a conventional F-theta lens with the vertical positioning of a telecentric lens for object space, ensuring the emerging laser beam is always perpendicular to the target surface across the entire scan field.

Since the diameter of the laser spot is 70 μ m and the laser moves at high speed during scanning, which is typical for the SLM process, the space between successive hatches must be considered when measuring the ED. Therefore, the ED [J/mm²] can be defined as defined in Eq. (1), where P, v, and h denote the laser power [W], scanning speed [mm/s], and hatch distance [mm], respectively.

$$ED = \frac{P}{v \cdot h}.\tag{1}$$

2.4 Manufacturing Parameters

Laser power, scanning speed, and layer thickness were varied to investigate their effects on the fusion of pure Mg and the potential for sample fabrication. As Mg has low melting and boiling points, the experiments began with low laser power combined with four different scanning speeds. Thus, the ED varied with scanning speed, while laser power remained constant. Subsequently, the laser power was gradually increased from 10 W to 40 W, as shown in Table 1, and combined with four different scanning speeds. Consequently, the ED also changed, ranging from 0.95 J/mm² to 4.29 J/mm². The ED played a significant role in the melting process of Mg and was therefore considered an important fabrication parameter. The hatch distance and layer thickness were kept constant in the initial stage of the study at 35 µm and 50 µm, respectively. Three samples were fabricated for each testing condition.

The most important factor in determining the useful range of parameters is the density of the samples. The proportion of smog formation is also considered. With some parameters, a higher density product can be achieved, but smog formation can cause deterioration in melting at higher scan ranges. A high level of smog in the processing chamber causes the laser rays to be reflected more strongly by the airborne powder particles. Increased vapor also absorbs more of the laser energy, which ultimately prevents the laser beams from reaching the powder bed.

After observing and analyzing the fusion behavior and density results in the first step of the study, the laser power was increased in the second step while maintaining the scanning speeds listed in Table 2. Since higher laser power led to better fusion results and product densities, higher laser powers were selected to analyze their effects. However, scanning speed can also have a significant influence. Therefore, in the second step of the study, the most effective scanning speeds were combined with the increased laser powers. Although scanning speeds of 400 mm/s, 600 mm/s, and 800 mm/s at 40 W resulted in good densities, 400 mm/s, 500 mm/s, and 600 mm/s were chosen at laser powers of 55 W, 65 W, and 75 W, respectively, due to the high ED induction.

Table 1. Manufacturing parameters in the first step of the study

Sample number	Laser power [W]	Scanning speed [mm/s]	Hatch spacing [mm]	Layer thickness [mm]	ED [J/mm²]	Product density [g/cm ³]	Relative density [%]
I-1	10	100	0.035	0.050	2.86	-	-
I-2	10	200	0.035	0.050	1.43	-	-
I-3	10	300	0.035	0.050	0.95	-	-
I-4	10	400	0.035	0.050	0.71	-	-
I-5	20	150	0.035	0.050	3.81	-	-
I-6	20	200	0.035	0.050	2.86	-	-
I-7	20	300	0.035	0.050	1.90	-	-
I-8	20	400	0.035	0.050	1.43	-	-
I-9	30	200	0.035	0.050	4.29	-	-
I-10	30	300	0.035	0.050	2.86	-	-
I-11	30	400	0.035	0.050	2.14	-	-
I-12	30	500	0.035	0.050	1.71	-	-
I-13	40	300	0.035	0.050	3.81	-	-
I-14	40	400	0.035	0.050	2.86	1.65	94.91
I-15	40	600	0.035	0.050	1.90	1.61	92.68
I-16	40	800	0.035	0.050	1.43	1.39	80.18

Table 2. Manufacturing parameters in the second step of the study

Sample number	Laser power [W]	Scanning speed [mm/s]	Hatch spacing [mm]	Layer thickness [mm]	ED [J/mm²]	Product density [g/cm ³]	Relative density [%]
II-1	55	400	0.035	0.050	3.93	-	-
II-2	65	500	0.035	0.050	3.71	-	-
II-3	75	600	0.035	0.050	3.57	-	-

In the second step of the study, a large amount of smoke and smog was observed when using high laser power and relatively low scanning speed. The lower scanning speed resulted in a high ED. Consequently, the samples were not produced satisfactorily. Therefore, higher scanning speeds were used in the third step of the study to reduce the ED, while the laser power remained the same as in the previous step. These parameters are listed in Table 3.

Table 3. Manufacturing parameters in the third step of the study

Sample number	Laser power [W]	Scanning speed [mm/s]	Hatch spacing [mm]	Layer thickness [mm]	ED [J/mm²]	Product density [g/cm ³]	Relative density [%]
III-1	55	700	0.035	0.050	2.24	1.65	94.96
III-2	65	700	0.035	0.050	2.65	1.67	95.95
III-3	75	750	0.035	0.050	2.86	1.68	96.51

Higher laser powers and their adjustable scanning speeds did not yield improved results. Therefore, the optimal laser power and scanning speeds identified in previous studies were used in the fourth step of the study, where a lower layer thickness was selected. As 800 mm/s at a laser power of 40 W resulted in low product density, a reduced scanning speed of 700 mm/s was chosen for this step, as shown in Table 4. These parameters were selected to observe

the effects of different layer thicknesses and the laser absorption characteristics of the powder bed and its top surface.

Table 4. Manufacturing parameters in the fourth step of the study

Sample number	Laser power [W]	Scanning speed [mm/s]	Hatch spacing [mm]	Layer thickness [mm]	ED [J/mm²]	Product density [g/cm ³]	Relative density [%]
IV-1	40	400	0.035	0.025	2.86	1.54	88.66
IV-2	40	500	0.035	0.025	2.29	1.55	89.34
IV-3	40	600	0.035	0.025	1.90	1.55	89.16
IV-4	40	700	0.035	0.025	1.63	1.55	89.04

2.5 Analysis of Product Properties

The densities were measured on samples that were well fused and capable of providing accurate results. When ethanol was used as a liquid, Archimedes' principle was applied to determine the densities. The weight of each sample was measured in air and then while immersed in the liquid, with an error margin of ± 0.0001 g, to calculate the density. The measurement was performed six times to improve the accuracy of the results. Three-dimensional images of the solid and pore zones of the materials were obtained using a ZEISS Xradia 620 Versa nano-computed tomography (nano-CT) scanner (Germany). The porosity of the samples was also observed with a scanning electron microscope (SEM) from Carl Zeiss (Germany), after the samples had been ground 1 mm from the vertical surface and then polished.

3 RESULTS AND DISCUSSION

3.1 Effect of Lower Laser Powers

The powder particles were not well fused at the low laser powers of 10 W and 20 W, even though the energy density was sufficient at lower scanning speeds. At a laser power of 30 W, the particles were adequately fused at scanning speeds of 200 mm/s and 300 mm/s; however, some layers were distorted and delaminated, as shown in Fig. 2. With a further increase in scanning speed to 400 mm/s and 500 mm/s at 30 W laser power, fusion did not occur. Therefore, the samples fabricated using 10 W to 30 W laser power were unsuitable for further studies such as density and porosity measurements.

There are several possible reasons for these results with 10 W to 30 W laser powers. The main reasons may be the low absorption of laser rays by the powder bed and the obstruction of the rays by the dense smog cloud. In laser—material interaction, most laser rays are typically reflected from the top surface of the powder layer [35]. Furthermore, magnesium is a shiny grey metal, which increases this reflection. The process is illustrated by the schematic diagram in Fig. 3a. Therefore, although the power was sufficient, only a small fraction of the laser rays was absorbed by the powder bed. After entering the powder bed, the rays are reflected multiple times within it [36]. The reflection and absorption are shown schematically in Fig. 3b. However, the low laser power of 10 W to 20 W was not sufficient to heat and melt the powder particles.

As the laser power increased to 30 W, the laser rays were sufficient to raise the temperature of the powder bed above 650 °C and melt the powder. Scanning speeds of 200 mm/s and 300 mm/s at 30 W laser power allowed enough time to melt the particles. Although melting occurred due to the greater number of laser rays penetrating the powder layer, as shown in Fig. 3b, the melt pool did not form sufficiently to agglomerate the layers and scan tracks. Therefore, it can be assumed that some areas were melted while others were not.

As a result, some plate formation and shifting were observed, as shown in Fig. 2. The plates were shifted by the recoater movement. With a further increase in scanning speed, sintering among the powder particles occurred. Consequently, soft cubic samples were formed at scanning speeds of 400 mm/s and 500 mm/s. These were destroyed during powder removal and detachment from the support structures. Eventually, an increase in scanning speed resulted in better melting.

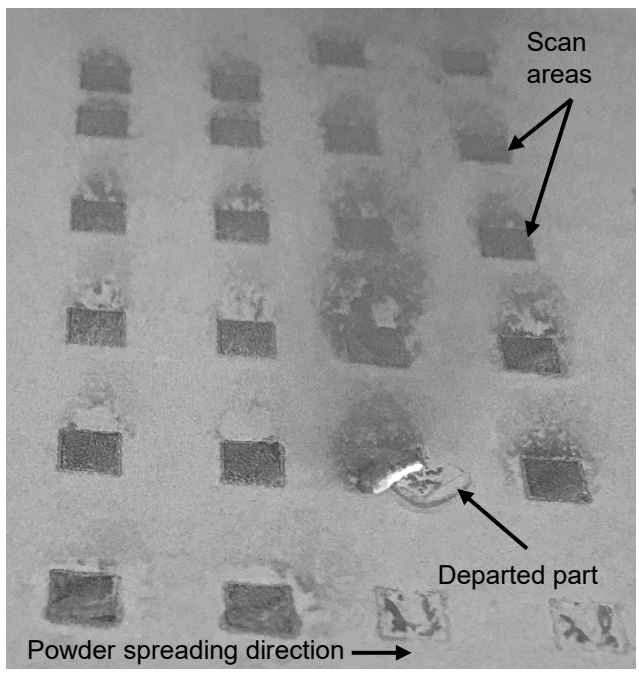


Fig. 2. A photograph during scanning

A large amount of smog was observed in the processing chamber during laser scanning. Although the smog was not detected by any sensor, only the observations made during production are discussed here. Smoke and particle detectors could provide more quantitative results and better control over the melting process. Therefore, it can be assumed that this smog also affects the amount of laser power reaching the powder bed. The smog formed from evaporated and combusted materials and powder particles [37,38]. As Mg has a low melting point and is prone to oxidation, it evaporated and burnt significantly. In addition, due to the cyclone effect above the action zone and the significantly low mass of Mg, the powder particles were easily lifted and mixed into the cyclone, as schematically represented in Fig. 3d. Moreover, powder explosions occurred in the powdered zone due to the expansion of inter-particle inert gas [37]. Consequently, a dense cloud formed above the action zone, with a high probability of impeding the laser from reaching the powder bed. At this point, higher laser power could escape this smog cloud. As a result, higher scanning speeds led to the formation of soft cubes at 30 W laser power.

A further increase in laser power to 40 W enabled the fabrication of some samples, whereas the lowest scanning speed of 300 mm/s did not produce any samples. At higher scanning speeds, however, some good cubes were formed with measurable densities. The laser power of 40 W delivered sufficient energy into the powder layer for good fusion to begin, as shown in Fig. 3c. As discussed, the lower scanning speed did not allow sufficient time to move forward to avoid the smog cloud. When the scanning speed increased to 400 mm/s, better melting occurred. Gradually increasing the scanning speed to 500 mm/s and 600 mm/s resulted in better melting than at 300 mm/s, even though the energy density was higher at the lower scanning speed.

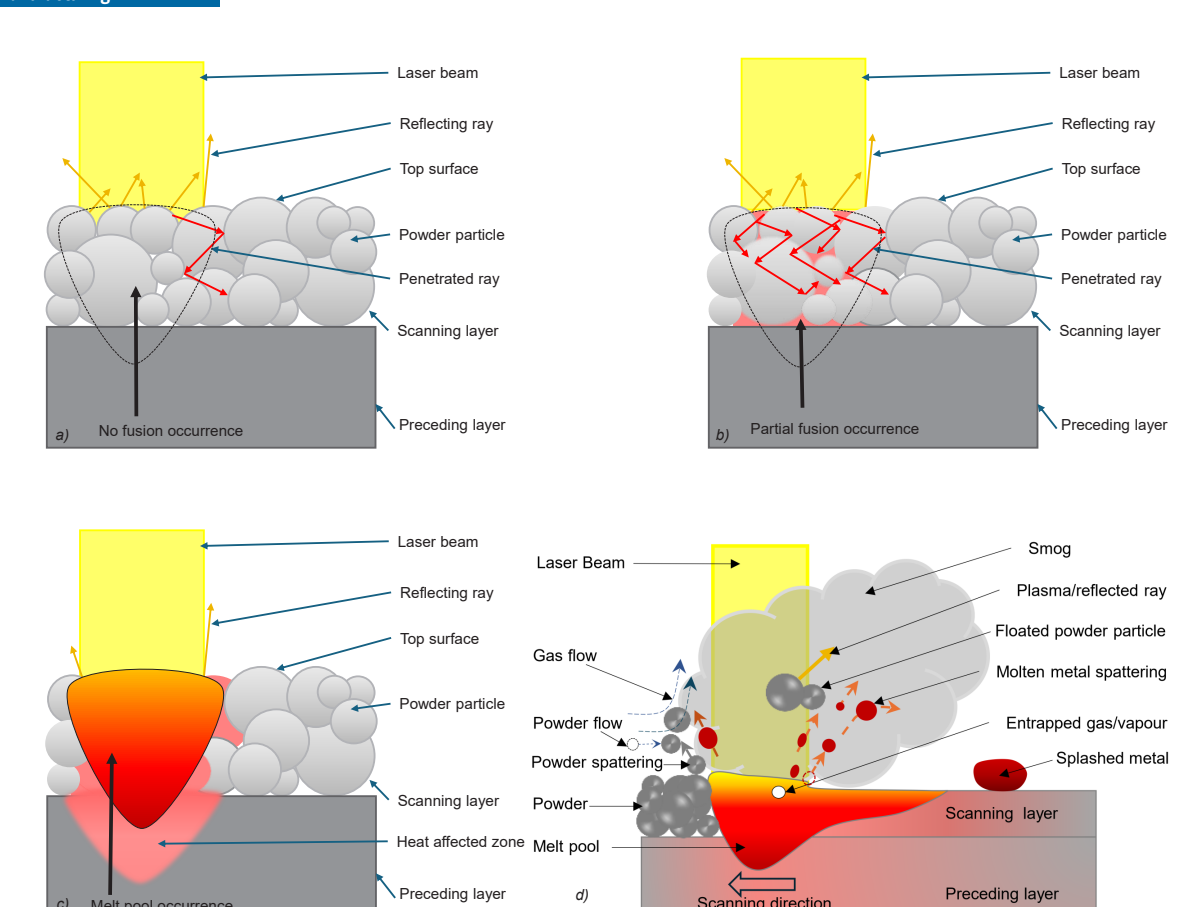


Fig. 3. Fusion characteristics; a) fusion with low laser power, b) fusion with medium laser power, c) melt pool formation with high laser power, and d) smog formation

However, the product density decreased at higher scanning speeds from 400 mm/s to 800 mm/s due to the significantly lower energy density.

There is also a possibility of high ED formation in the melt pool at a low scanning speed of 300 mm/s, which may cause instability in the melt pools and result in melt spattering [39], as shown in Fig. 3d. Additionally, trapped gas bubbles and metal vapor caused explosions in the melt pools [40]. This resulted in significant metal splashes, causing the action zones to lose material. Conversely, the splashed material fell onto the scan area and created some bumpy zones. The loss of material in one area led to an accumulation of powder

particles in the subsequent layer at that location, resulting in a higher powder layer height. Consequently, the subsequent layer could not fuse well or form a uniform melt pool, as shown in the SEM images in Fig. 4. This led to insufficient bonding with the previous layer and the formation of a pore. To observe this phenomenon, the sample fabricated with 60 W laser power, 700 mm/s scanning speed, 0.035 mm hatch spacing, and 0.050 mm layer thickness is shown in Fig. 4.

Figure 4 shows that some layers are affected by the phenomena described above. These layers are significantly influenced by highly irregular melt pool and pore formation. Several of these layers are marked by two parallel lines in Fig. 4. These pores also influenced

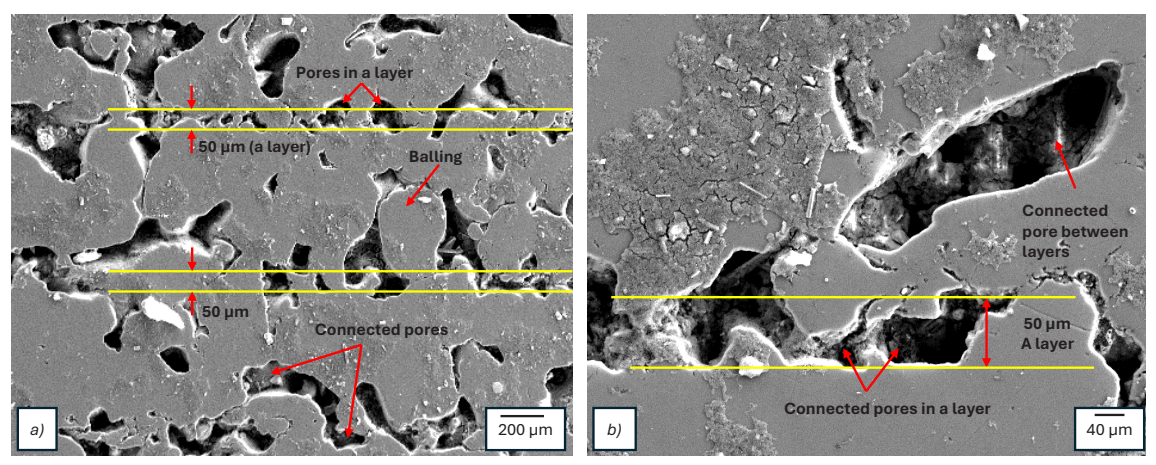


Fig. 4. Common pore characteristics of the samples; a) overall pore formation, with some layers exhibiting high pore content, and b) higher magnification image of the pores in a layer with high pore content

pore formation in subsequent layers. Some pores extended across several layers, forming connected pores between them. Additionally, part of the last scanned layer may exhibit uneven areas due to the deposition of spattered particles and the formation of spheres caused by the balling effect, as shown in Fig. 4a. As a result, this part had to be removed and displaced from the specific manufacturing location by the recoater movement. Ultimately, the combination of 40 W laser power and 300 mm/s scanning speed produced disorganized samples. Therefore, density was not determined for samples produced with these manufacturing parameters.

Comparing the effects of laser power between samples I-5 and I-13, it can be seen that despite the same high ED of 3.81 J/mm², no melting occurs in I-5, while high temperatures and significant spattering of molten metal occur in I-13. The heating rate (scanning speed) played an important role in the fusion mechanisms. Since the ED was very high, there is a high probability that strong vaporization began at the top of the powder bed. After the onset of vaporization, the penetration of the laser beam decreased due to obstruction by the vapor cloud, resulting in insufficient melting of sample I-5. When the scanning speed was increased at the same ED, the laser left the action zone after supplying higher energy in less time. This allowed for a higher probability of melting and a greater energy content in the melt pools. Therefore, a high ED led to high temperatures and a reduction in the viscosity of the melt pools, resulting in spattering of molten metal in sample I-13. To investigate these phenomena in more detail, the part with the lowest density was analyzed using a nano-CT scan and explained with the help of Fig. 5.

Comparing samples I-1, I-6, I-10, and I-14, which have the same ED (2.86 J/mm²) but different laser powers (10 W, 20 W, 30 W, and 40 W), it can be observed that while 10 W to 30 W could not produce a good sample, 40 W resulted in the highest density. Even the significantly low ED of 1.43 J/mm² was sufficient to fabricate a good sample with a laser power of 40 W. In contrast, the same ED of 1.43 J/mm² and higher EDs could not produce a sample when the laser powers were below 40 W. It is therefore clear that lower laser powers perform worse due to insufficient absorption of the laser rays by the powder bed. Here, a good sample refers to one that is well formed with a cubic structure and whose product density can be measured, while other samples are not well formed or fused and do not form a cube.

Since I-16 has the lowest product density among the well-formed samples, this research has taken this sample into account to study the formation and behavior of melt pools. To investigate the effects of the laser parameters and the formation of melt pools, the product with the lowest density was selected. This can provide an indication of the melting mechanism, even if the product was not well manufactured. Therefore, this sample was analyzed with nano-CT scanning and is shown in Fig. 5. The light grey and dark grey areas represent the solid and porous regions, respectively. Successive images are taken at intervals of 5 μ m through the vertical direction, which is the build-up direction of the sample. Examining these images, it can be seen that the pores are interconnected. It is also clear that they have irregular shapes, and their sizes vary accordingly.

Based on the pores of sample I-16 and the consolidated patches, certain melting characteristics of this sample can be determined. This indicates that the track was not laid down evenly throughout. There are occasional fluctuations in the melt pools of the track [25]. The pores also varied in size in each direction. Consequently, the density varied both between the layers and between the tracks. For example, the three strips -1, -2, and -3 marked in Fig. 5 can be considered to investigate their melting properties. The width of the stripes is 100 µm, and these stripes can be visualized in all images. However, the region in strip-1 has a higher density than the region in strip-3, indicating that fusion was better in some areas, while in others less material was obtained, and pores were formed. Although this is one possible cause for such melting properties and the formation of porosity, other factors may also contribute. It is an inherent characteristic of SLM that some action zones melt well and form a good melt pool, while others may suffer from lack of melting or spattering of molten metal. This can also be influenced by the different size distribution of the powder particles and the varying powder packing from place to place.

The shape of a melt pool can be understood from any dot (with a small surrounding area) placed on a figure panel in Fig. 5. For example, a red dot is placed on each panel representing the same scan area. Since the following images represent the 5 µm above in the build direction, the same area or location shows the variation of the melt pool in the vertical direction. However, the red dot originated from a pore area that eventually filled with material as it moved in the vertical direction. Similarly, one can visualize and examine the pore and solid zones, which provides insight into the melting properties. As mentioned earlier, these porosities result from evaporation, combustion, material loss, material spattering, and laser shielding by smog [32]. On the other hand, a large number of round patches of solid material in the cross-section of the sample match the section size of the powder particles and could indeed be unmelted powder particles. Better stabilization of the melt pools is required to maximize density. A higher laser power may be preferable to achieve the desired melt pool properties.

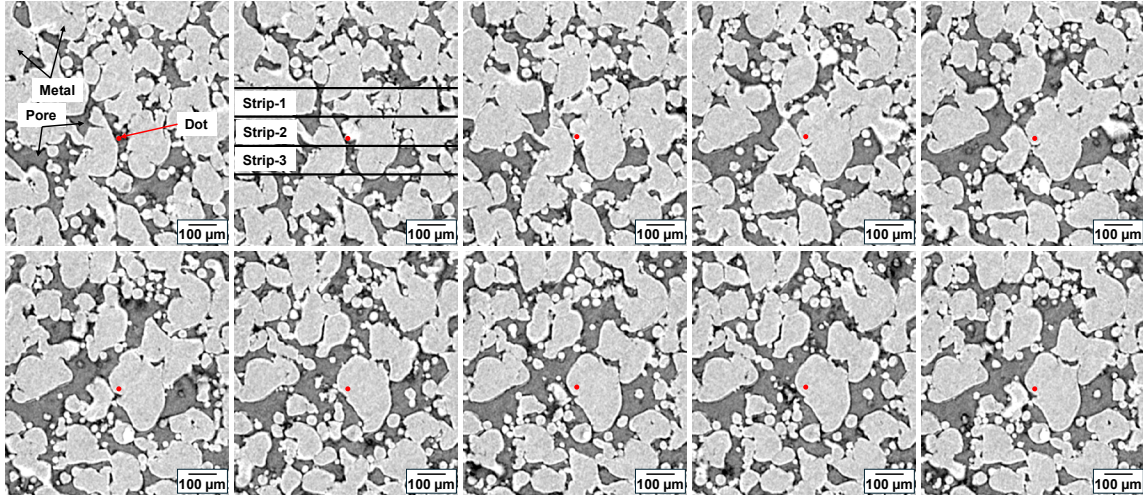


Fig. 5. Nano-CT scanned images showing pores and metallic zones

3.2 Effects of High Laser Powers

As the increase in laser power supported an improved fusion process during manufacturing and resulted in higher product density, the laser power was further increased in the second stage of the study. However, since scanning speed significantly affects the fusion process, the speeds were selected based on findings from the previous study. High ED also led to increased fume and smog generation in the manufacturing chamber. Therefore, to maintain the ED, a scanning speed of 400 mm/s to 600 mm/s was chosen for the second stage. It was observed that higher laser power produced better melt pools; for example, 40 W was more effective than 30 W, although both generated considerable smog. Additionally, although increased vaporization from the top of the powder bed is possible, the resulting vapor also impedes effective laser penetration. Therefore, higher laser power at the outset can lead to excessive energy deposition. The proportion of laser rays reaching the powder bed decreases as vaporization begins. Accordingly, higher laser power can result in improved melt pool formation. With this in mind, a higher laser power was selected for further investigation.

The densities of some samples in the second stage are lower than those prepared with 40 W laser power for samples I-14 to I-16, and some are not well fabricated. Therefore, the densities of these samples cannot be reported. The second stage of the experiment showed strong smog formation in the fabrication chamber. The smog reflected the laser rays even above the intended scanning layer. As a result, insufficient energy was delivered in many areas, which also contributed to a high level of pore formation. However, due to the high laser power, a significant amount of Mg was burnt and vaporized. As previously mentioned, this also created a cyclone above the

powder bed, which drew in many Mg powder particles and formed a protective shield. This shield prevented the laser from penetrating the powder layer. Many sparks were observed with the increased number of powder particles in the cyclone, as shown in Fig. 3d. It can be assumed that the laser struck the particles and caused the sparks. As a result, the amount of melting was insufficient to form a good melt pool. Additionally, the formation of smoke, the vaporization of the metal, and the removal of powder particles caused metal loss from the action zone [38]. Consequently, the density decreased, and the samples were damaged during production.

3.3 Effects of High Laser Powers with Higher Scanning Speeds

Since lower scanning speeds combined with higher laser powers resulted in a high ED, the scanning speed was increased in the third step of the study. As a result, the samples were well prepared, as shown in Fig. 6a. Additionally, the densities of the samples increased in this step, as shown in Fig. 6b. When the laser power was lowest at 55 W (in sample III-1) in the third step, the resulting density was low (1.62 g/cm³). However, when the laser power was increased to 65 W and the scanning speed was kept constant at 700 mm/s, the resulting density in sample III-2 increased to 1.63 g/cm³. In sample III-3, which was fabricated with a higher laser power (75 W) and scanning speed (750 mm/s), the density was even higher.

Since a high ED occurred in sample II-1 due to the lower scanning speed compared to sample III-3, a large amount of smog was generated. When the scanning speed was increased at the same laser power, the ED decreased, and fusion and melt pool formation improved. This resulted in successful sample fabrication with high density. The smog and fumes were much lower compared to the

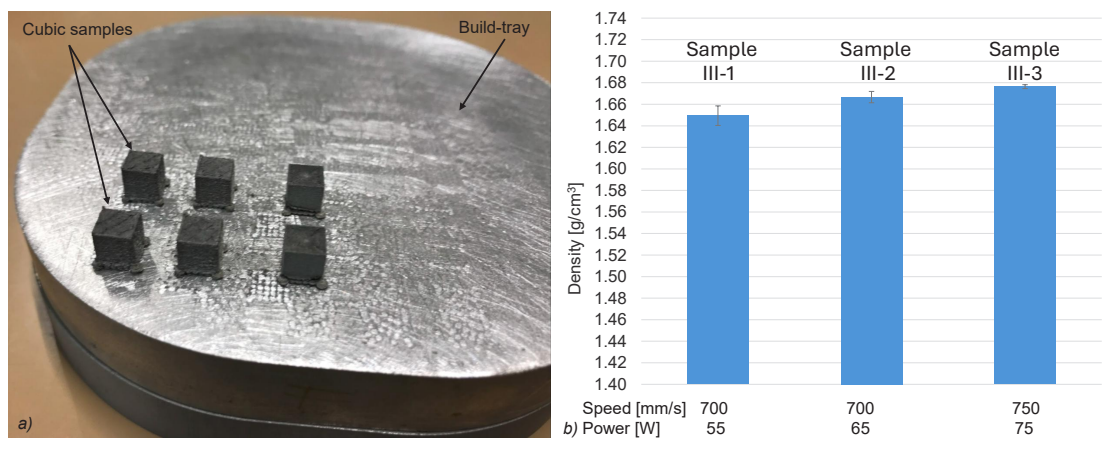


Fig. 6. Samples and density results in the third step of the study; a) photograph of the cubic samples on the build tray; and b) densities

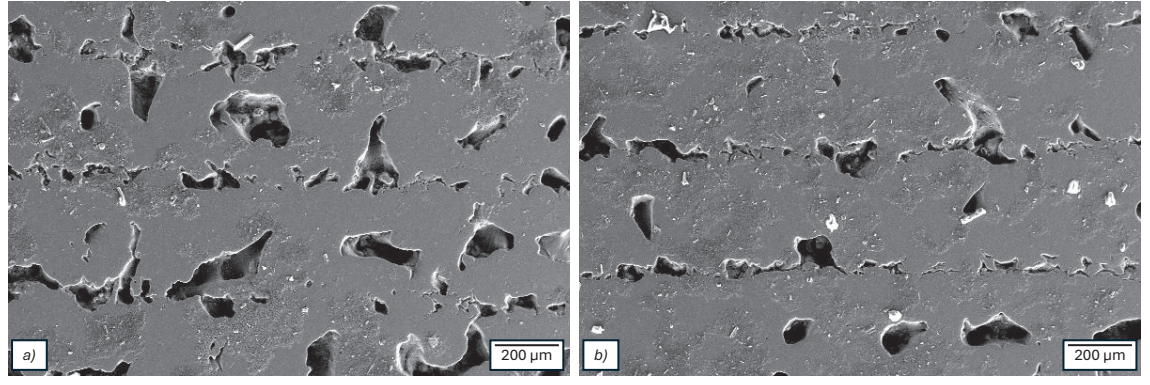


Fig. 7. Difference in porosity; a) sample fabricated with a laser power of 70 W and a scanning speed of 750 mm/s; and b) sample fabricated with a laser power of 80 W and a scanning speed of 800 mm/s

second step of the study. However, increasing the laser power from 55 W to 65 W improved the quality of the melt pools, as indicated by the increase in density. This was confirmed by SEM examinations of other samples produced with a laser power of 70 W and a scanning speed of 750 mm/s, and with a laser power of 80 W and a scanning speed of 800 mm/s, while keeping the other parameters constant. The SEM images of the vertical cross-sections of these samples are shown in Fig. 7.

The SEM images in Fig. 7 clearly show that the quality of the melt pools improved as the laser power increased, reducing gaps between tracks and decreasing pores. Therefore, higher laser power combined with a slightly higher scanning speed helped to melt the powder more effectively and form a better melt pool in sample III-3 compared to sample II-3. As the EDs in the third step of the study were within an appropriate range, less fume and smog were observed.

3.4 Effect in Decreasing the Layer Thickness

By reducing the layer thickness to 25 μ m, the density results were slightly lower than those for samples with a higher layer thickness of 50 μ m. In the fourth step of the study, the densities were almost the same for all samples, as shown in Fig. 8. Smog formation was almost identical to that of samples fabricated with the same laser power (40 W) in the first step of the study, except at the lowest scanning speed (300 mm/s). As the scanning speed in the fourth

step was within the optimal range, smog formation was low. This was due to the uniform effects on the top of the powder layer. As the layer thickness decreased, the total energy input to the powder layer increased, which also increased the thermal energy in the melt pools. This led to a lower viscosity of the melt, resulting in instability of the melt pools and spattering of molten metal [39]. Therefore, the action zone lost more material than the previous samples produced at $50 \ \mu m$. As a result, the overall density of the samples decreased.

The melting mechanism and the effects of smog can be visualized by examining pore formation in one of the samples, which was produced with a layer thickness of 25 µm. Fig. 8b to d shows the nano-CT images of sample IV-1, which are vertical cross-sectional planes arranged sequentially at intervals of several hundred micrometers. The proportion of pores is visible in these images, indicating that they contain a low, medium, and high proportion of pores, respectively. The density therefore varied significantly within the same scanning layer. In some areas, there was good fusion and stabilized melt pool formation, while in others there was low laser energy or an unstable melt pool with high thermal energy. The smog obstructed the laser, resulting in low energy deposition on the powder bed. As the energy decreased, evaporation also decreased, causing the laser to fall onto the powder bed. When the melt pools accumulate higher energy, the viscosity of the melt may decrease, which can lead to destabilization of the melt pools. This can eventually result in spattering and material loss.

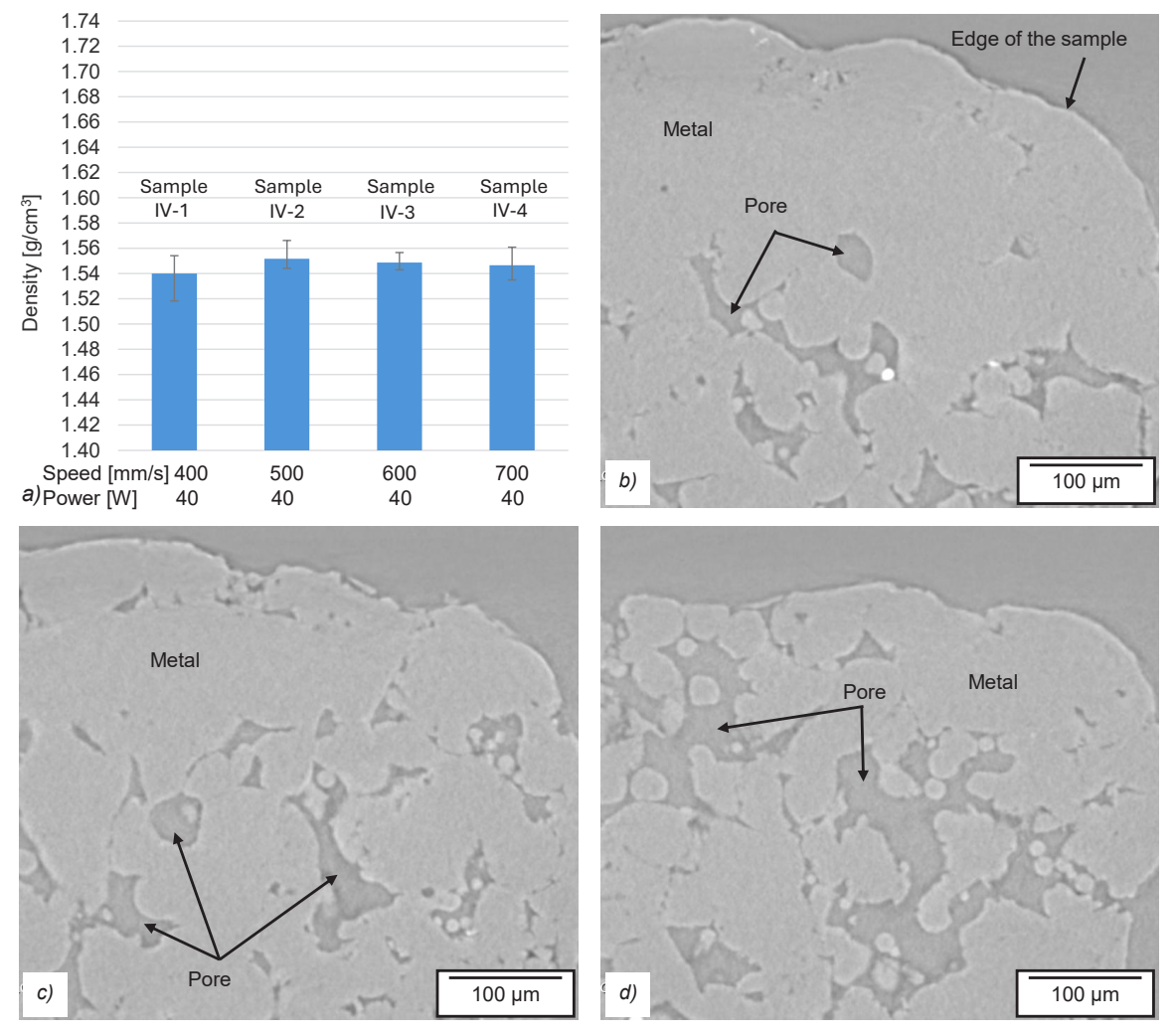


Fig. 8. Densities and porosities of the sample fabricated in the fourth step of the study; a) densities; b) low-porosity site; c) medium-porosity site, and d) high-porosity site

4 CONCLUSIONS

This article investigates and describes the melting properties of magnesium during selective laser melting. The following characteristics are observed and demonstrated using density measurements, as well as images from nano-CT scans and SEM of the samples.

Low laser power is insufficient to melt the powder particles and connect the layers and tracks, even when the ED is the same as with higher laser power. At the same ED, the scanning speed must be increased, which is the main advantage in melting the powder and forming a melt pool. This is due to the ability to avoid the smog clouds formed by the vaporization of materials at the top of the powder bed. The forward movement after the penetration of sufficient energy within a short time results in better fusion. A slower scanning speed with lower power does not provide enough energy before a dense cloud forms and prevents the laser beams from reaching the powder bed.

A high ED causes melt pool instability due to the explosion of melt pools and spattering, resulting in insufficient material and the formation of voids or the inability to form a product. Although reducing the layer thickness enables better melting in some areas, in other areas there is instability in the melt pools, which also worsens the overall density.

References

- [1] Zhang, W, Xu, J. Advanced lightweight materials for Automobiles: A review. Mater Des 221 110994 (2022) D0I:10.1016/j.matdes.2022.110994.
- [2] Ng, C.C., Savalani, M., Man, H.C. Fabrication of magnesium using selective laser melting technique. Rapid Prototyp J 17 479-490 (2011). D0I:10.1108/13552541111184206.
- [3] Blanco, D., Rubio, E.M., Lorente, R., Sáenz-Nuño, M.A. Lightweight structural materials in open access: Latest trends. *Materials* 14 6577 (2021) DOI:10.3390/ ma14216577.
- [4] Tiyyagura, H.R., Mohan, T., Pal, S., Mohan, M.K. Surface modification of Magnesium and its alloy as orthopedic biomaterials with biopolymers. Balakrishnan, P., Sreekala, M.S., Sabu T. (eds) Fundamental Biomaterials: Metals, Elsevier 197-210 (2018) DOI:10.1016/B978-0-08-102205-4.00009-X.
- [5] Yang, Y., Wu, P., Lin, X., Liu, Y., Bian, H., Zhou, Y., et al. System development, formability quality and microstructure evolution of selective laser-melted magnesium. Virtual Phys Prototyp 11 173-181 (2016) D0I:10.1080/17452759.2 016.1210522.
- [6] Fard, M.G., Sharifianjazi, F., Kazemi, S.S., Rostamani, H., Bathaei, M.S. Laser-based additive manufacturing of magnesium alloys for bone tissue engineering applications: From chemistry to clinic. J Manuf Mater Process 6 158 (2022) D0I:10.3390/jmmp6060158.
- [7] Prakasam, M., Locs, J., Salma-Ancane, K., Loca, D., Largeteau, A., Berzina-Cimdina, L. Biodegradable materials and metallic implants-A review. J Funct Biomater 8 44 (2017) D0I:10.3390/jfb8040044.
- [8] Manakari, V., Parande, G., Gupta, M. Selective laser melting of magnesium and magnesium alloy powders: A review. Metals 7 2 (2017) D0I:10.3390/met7010002.
- [9] Prasad, S.V.S., Prasad, S.B., Verma, K., Mishra, R.K., Kumar, V., Singh, S. The role and significance of Magnesium in modern day research-A review. *J Magnes Alloy* 10 1-61 (2022) D0I:10.1016/j.jma.2021.05.012.
- [10] Zagórski, I. Surface roughness evaluation of AZ31B magnesium alloy after rough milling using tools with different geometries. Stroj Vestn-J Mech E 70 355-368 (2024) D0I:10.5545/sv-jme.2023.885.
- [11] Staiger, M.P., Pietak, A.M., Huadmai, J., Dias, G. Magnesium and its alloys as orthopedic biomaterials: A review. *Biomaterials* 27 1728-1734 (2006) D0I:10.1016/j.biomaterials.2005.10.003.
- [12] Kirkland, N.T., Birbilis, N., Staiger, M.P. Assessing the corrosion of biodegradable magnesium implants: A critical review of current methodologies and their limitations. Acta Biomater 8 925-936 (2012) D0I:10.1016/j.actbio.2011.11.014.
- [13] Gu, X.N., Zheng, Y.F. A review on magnesium alloys as biodegradable materials. Front Mater Sci China 4 111-115 (2010) D01:10.1007/s11706-010-0024-1.
- [14] Munsch, M. Laser additive manufacturing of customized prosthetics and implants for biomedical applications. Brandt, M. (ed.) Laser Additive Manufacturing 399-420 (2017) D0I:10.1016/B978-0-08-100433-3.00015-4.

- [15] Persaud-Sharma, D., Mcgoron, A. Biodegradable magnesium alloys: A review of material development and applications. J Biomim Biomater Tissue Eng 12 25-39 (2012) D0I:10.4028/www.scientific.net/JBBTE.12.25.
- [16] Gray, J.E., Luan, B. Protective coatings on magnesium and its alloys A critical review. J Alloys Compd 336 88-113 (2002) D0I:10.1016/S0925-8388(01)01899-0
- [17] Kiani, F., Wen, C., Li, Y. Prospects and strategies for magnesium alloys as biodegradable implants from crystalline to bulk metallic glasses and composites-A review. Acta Biomater 103 1-23 (2020) D0I:10.1016/j.actbio.2019.12.023.
- [18] DebRoy, T., Wei, H.L., Zuback, J.S., Mukherjee, T., Elmer, J.W., Milewski, J.O., et al. Additive manufacturing of metallic components Process, structure and properties. *Prog Mater Sci* 92 112-224 (2018) D0I:10.1016/j. pmatsci.2017.10.001.
- [19] Gotlih, J., Karner, T., Belšak, R., Ficko, M., Berus, L., Brajlih, T., et al. Design and manufacturing of conformal cooling channels for injection molding: A review. Karabegovic, I., Kovačević, A., Mandzuka, S. (eds.) Lect Notes Networks Syst 687 156-169 (2023) Cham Springer D0I:10.1007/978-3-031-31066-9_17.
- [20] Drstvenšek, I., Zupanič, F., Bončina, T., Brajlih, T., Pal, S. Influence of local heat flow variations on geometrical deflections, microstructure, and tensile properties of Ti-6Al-4 V products in powder bed fusion systems. J Manuf Process 65 382-396 (2021) D0I:10.1016/j.jmapro.2021.03.054.
- [21] Pal, S., Gubeljak, N., Hudák, R., Lojen, G., Rajťúková, V., Brajlih, T., et al. Evolution of the metallurgical properties of Ti-6Al-4V, produced with different laser processing parameters, at constant energy density in selective laser melting. Results Phys 17 103186 (2020) D0I:10.1016/j.rinp.2020.103186.
- [22] Pal, S., Bončina, T., Lojen, G., Brajlih, T., Švara Fabjan, E., Gubeljak, N., et al. Fine martensite and beta-grain variational effects on mechanical properties of Ti-6Al-4V while laser parameters change in laser powder bed fusion. *Mater Sci Eng A* 892 146052 (2024) DOI:10.1016/j.msea.2023.146052.
- [23] Kjer, M.B., Pan, Z., Nadimpalli, V.K., Pedersen, D.B. Experimental analysis and spatial component impact of the inert cross flow in open-architecture laser powder bed fusion. J Manuf Mater Process 7 143 (2023) D0I:10.3390/jmmp7040143.
- [24] Wischeropp, T.M., Emmelmann, C., Brandt, M., Pateras, A. Measurement of actual powder layer height and packing density in a single layer in selective laser melting. Addit Manuf 28 176-183 (2019) D0I:10.1016/j.addma.2019.04.019.
- [25] Shrestha, S., Chou, K. Residual heat effect on the melt pool geometry during the laser powder bed fusion process. J Manuf Mater Process 6 153 (2022) D0I:10.3390/immp6060153.
- [26] Babič, M., Kovačič, M., Fragassa, C., Šturm, R. Selective laser melting: A novel method for surface roughness analysis. Stroj Vestn-J Mech E 70 313-324 (2024) D0I:10.5545/sv-jme.2024.1009.
- [27] Pal, S., Lojen, G., Hudak, R., Rajtukova, V., Brajlih, T., Kokol, V., et al. As-fabricated surface morphologies of Ti-6Al-4V samples fabricated by different laser processing parameters in selective laser melting. Addit Manuf 33 101147 (2020) D0I:10.1016/j.addma.2020.101147.
- [28] Patil, V.V., Mohanty, C.P., Prashanth, K.G. Parametric optimization of selective laser melted 13Ni400 maraging steel by Taguchi method. *J Manuf Mater Process* 8 52 (2024) D0I:10.3390/jmmp8020052.
- [29] Pal, S., Lojen, G., Drstvenšek, I. Microstructural phase transformation evolution of Ti-6Al-4V alloy in selective laser melting process. Metall Mater Eng Congr South-East Eur 26 (2017).
- [30] Ahmadi, M., Tabary, S.A.A.B., Rahmatabadi, D., Ebrahimi, M.S., Abrinia, K., Hashemi, R. Review of selective laser melting of magnesium alloys: advantages, microstructure and mechanical characterizations, defects, challenges, and applications. J Mater Res Technol 19 1537-1562 (2022) D0I:10.1016/j.jmrt.2022.05.102.
- [31] Shen, H., Yan, J., Niu, X. Thermo-fluid-dynamic modeling of the melt pool during selective laser melting for AZ91D magnesium alloy. *Materials* 13 4157 (2020) D0I:10.3390/ma13184157.
- [32] Ding, R., Yao, J., Du, B., Li, K., Li, T., Zhao, L., et al. Effect of shielding gas volume flow on the consistency of microstructure and tensile properties of 316I manufactured by selective laser melting. *Metals* 11 205 (2021) DOI:10.3390/met11020205.
- [33] Zeng, Z., Salehi, M., Kopp, A., Xu, S., Esmaily, M., Birbilis, N. Recent progress and perspectives in additive manufacturing of magnesium alloys. J Magnes Alloy 10 1511-1541 (2022) DOI:10.1016/j.jma.2022.03.001.
- [34] Hu, D., Wang, Y., Zhang, D., Hao L., Jiang, J., Li, Z., et al. Experimental Investigation on selective laser melting of bulk net-shape pure Magnesium. *Mater Manuf Process* 30 1298-1304 (2015) D0I:10.1080/10426914.2015.1025963.
- [35] Zhang, D., Wang, W., Guo, Y., Hu, S., Dong, D., Poprawe, R., et al. Numerical simulation in the absorption behavior of Ti6Al4V powder materials to laser

- energy during SLM. J Mater Process Technol 268 25-36 (2019) D0I:10.1016/j. jmatprotec.2019.01.002.
- [36] Tolochko, N.K., Mozzharov, S.E., Yadroitsev, I.A., Laoui, T., Froyen, L., Titov, V.I., et al. Balling processes during selective laser treatment of powders. *Rapid Prototyp J* 10 78-87 (2004) D0I:10.1108/13552540410526953.
- [37] Yadav, P., Rigo, O., Arvieu, C., Le Guen, E., Lacoste, E. In situ monitoring systems of the SLM process: On the need to develop machine learning models for data processing. Crystals 10 524 (2020) D0I:10.3390/cryst10060524.
- [38] Shan, X., Pan, Z., Gao, M., Han, L., Choi, J.P., Zhang, H. Multi-physics modeling of melting-solidification characteristics in laser powder bed fusion process of 316L stainless steel. Materials 17 946 (2024) D0I:10.3390/ma17040946.
- [39] Li, Z., Li, H., Yin, J., Li, Y., Nie, Z., Li, X., et al. A Review of spatter in laser powder bed fusion additive manufacturing: in situ detection, generation, effects, and countermeasures. *Micromachines* 13 1366 (2022) DOI:10.3390/mi13081366.
- [40] Yu, G., Gu, D., Dai, D., Xia, M., Ma, C., Chang, K. Influence of processing parameters on laser penetration depth and melting/re-melting densification during selective laser melting of aluminum alloy. *Appl Phys A Mater Sci Process* 122 891 (2016) D0I:10.1007/s00339-016-0428-6.

Acknowledgements The authors thank the Slovenian Research Agency for funding the research (Grant Nos. GC-0007 P2-0118, P2-0137, P2-0157 J1-2470, J1-2471, J1-4416, J7-4636, J7-50226, J7-50227, J1-60015 and J7-60120). The project is co-financed by the Republic of Slovenia, the Ministry of Education, Science and Sport, and the European Union through the European Regional Development Fund.

Received 2025-05-09, revised 2025-09-16, 2025-10-13, accepted 2025-10-13 as Original scientific paper 1.01.

Data availability The data that support the findings of this study are available from the corresponding author upon reasonable request.

Author contribution Snehashis Pal: Conceptualization, Methodology, Formal analysis, Investigation, Visualization, Writing—original draft; Matjaž Finšgar: Formal analysis, Investigation, Writing—review and editing; Jernej Vajda: Formal analysis, Investigation; Uroš Maver: Formal analysis,

Investigation; Tomaž Brajlih: Formal analysis, Investigation; Nenad Gubeljak: Formal analysis, Investigation; Hanuma Reddy Tiyyagura: Conceptualization, Formal analysis, Investigation, Writing—review and editing, Supervision; Igor Drstvenšek: Conceptualization, Formal analysis, Investigation, Writing—review and editing, Supervision.

Proces spajanja čistega magnezija med selektivnim laserskim taljenjem

Abstract V raziskavi smo proučevali obnašanje taljenja čistega magnezija in pretočnost njegove taline med selektvinim laserskim taljenjem. Raziskali smo tudi vpliv različnih kombinacij procesnih parametrov na povečanje gostote izdelka. Moč laserja smo postopoma povečevali in pri tem spreminjali hitrosti skeniranja za vsako serijo izdelkov, s čimer smo vplivali na vnos energije v talilni process (ED). Moč laserja se je gibala od 10 W do 75 W, hitrost skeniranja pa od 100 mm/s do 800 mm/s. Z nižjimi močmi laserja nismo dosegli zadovoljivega taljenja materiala, medtem ko so višje moči laserja povzročile boljše taljenje, z znatnimi razlikami tudi pri enakih vnosih energije - ED. Visoka energijska gostota - ED med 3,50 J/mm² in 4,30 J/mm² je povzročila pomanjkljivo taljenje pri nizki moči laserja oziroma nestabilen talilni bazen z znatnim pršenjem materiala pri visoki moči laserja. Nasprotno pa so zmerne ED v območju od 1,40 J/mm² do 2,90 J/mm² povzročile boljšo gostoto pri visoki moči laserja. Višje hitrosti skeniranja so pomagale preprečiti nastanek gostega oblaka smoga in s pomočjo večje laserske moči zagotovile zadostno energijo v kratkem času. Zato je povečanje tako laserske moči kot hitrosti skeniranja izboljšalo učinkovitost taljenja in povečalo gostoto vzorca. Relativna gostota vzorcev se je gibala od 80 % do 96,5 %. Zmanjšanje debeline plasti s 50 µm na 25 µm pri laserski moči 40 W je na nekaterih območjih povzročilo nastanek dobro oblikovanega bazena taline, na drugih pa znatno brizganje taline, kar je povzročilo poslabšanje gostote.

Ključne besede magnezij, talilni bazen, moč laserja, hitrost skeniranja, debelina plasti, nosilna struktura, lasersko taljenje praškastega sloja